JGR Solid Earth

RESEARCH ARTICLE
10.1029/2020JB020648

Over a Century of Sinking in Mexico City: No Hope for Significant Elevation and Storage Capacity Recovery

E. Chaussard[1], E. Havazli[2], H. Fattahi[2], E. Cabral-Cano[3], and D. Solano-Rojas[4]

[1]Department of Earth Sciences, University of Oregon, Eugene, OR, USA, [2]Jet Propulsion Laboratory, California Institute of Technology, Pasadena, CA, USA, [3]Instituto de Geofísica, Universidad Nacional Autónoma de México, México CDMX, Mexico, [4]División de Ingeniería en Ciencias de la Tierra, Facultad de Ingeniería, Universidad Nacional Autónoma de México, México CDMX, Mexico

Key Points:

- Integration of 115 years of deformation data reveals subsidence up 50 cm/year in Mexico City
- The majority of the subsidence is irreversible and its rates are linearly correlated to the thickness of the upper aquitard
- Migration of low-quality water to the productive aquifer sets the stage for a water crisis, which influences the socioeconomic landscape

Supporting Information:

Supporting Information may be found in the online version of this article.

Correspondence to:

E. Chaussard,
echaussard@gmail.com

Citation:

Chaussard, E., Havazli, E., Fattahi, H., Cabral-Cano, E., & Solano-Rojas, D. (2021). Over a century of sinking in mexico city: No hope for significant elevation and storage capacity recovery. *Journal of Geophysical Research: Solid Earth*, *126*, e2020JB020648. https://doi.org/10.1029/2020JB020648

Received 24 JUL 2020
Accepted 23 MAR 2021

Abstract Many areas worldwide are known to experience land subsidence due to groundwater extraction. It is traditionally assumed that subsidence extent and rates are controlled by groundwater extraction locations and volumes. Here, we reevaluate this assumption in the Mexico City metropolitan area by combining stratigraphic, hydrologic, geodetic, and demographic datasets. Integration of 115 years of leveling with 24 years of Interferometric Synthetic Aperture Radar (InSAR) and 14 years of GPS data reveals that subsidence rates have been mostly constant in Mexico City since at least 1950 and reach 50 cm/year. Analysis of InSAR and GPS data shows that no significant elastic deformation exists, demonstrating that the subsidence is almost fully irreversible. In Mexico City, no direct relationships exist between groundwater level fluctuations and subsidence rates or between pumping rates and subsidence rates. In contrast, a strong positive linear relationship is isolated between subsidence rates and the thickness of the upper aquitard. Through the integration of these long-term datasets, we forecast that it will take ~150 years to reach total compaction of the upper aquitard, which may lead to additional subsidence up to 30 m. With the potentiometric surface now deeper than most of the aquitard, clay's porewater rich in salts, chemical constituents, and pollutants is now flowing downward into the productive aquifer, hence decreasing water quality. Finally, our work shows that the consequences of land subsidence greatly influence the socioeconomic landscape in the Mexico City metropolitan area.

1. Introduction

Water sustainability is a major environmental problem impacting many metropolitan areas either in the form of flooding risks or lack of access to drinking water, but none are as affected as Mexico City. Mexico City (Ciudad de México or CDMX, formerly called the Federal District) is the capital of Mexico and the most populous city in North America. 9.2 million people live in CDMX and over 21 million live in its metropolitan area. The metropolitan area of the valley of Mexico (Zona Metropolitana del Valle de México, ZMVM), encompasses CDMX, part of the State of Mexico, and one municipality of the State of Hidalgo. The Zona Metropolitana del Valle de México (ZMVM) is the economic, financial, and political center of Mexico and is home to 17% of the national population, with an average of 92 persons per hectare, and contributes 23% of the national Gross Domestic Product (GDP) (Pojani & Stead, 2017). The ZMVM is a water paradox: the city has a long history of floods that prompted hydraulic management dating back to pre-Hispanic times, whereas a large amount of the city's freshwater needs nowadays to be brought from sources over 100 km away.

The ZMVM is located in an endorheic basin on the flatbed of what was once a large lake system with no natural drainage outlet at a base elevation of 2,200 m above sea level. This basin is surrounded by several mountain ranges part of the Mexican Volcanic Belt with elevations reaching over 5,000 m. Rain and spring water runoff from these elevated slopes to the West, East, and South of the basin collected in this depression and became saline due to evaporation, forming the former lake Texcoco (Figure 1a). The prehispanic city of Tenochtitlán (now Mexico City) was founded by the Aztecs on lake Texcoco in 1325. In the 1520s, after the Spanish conquest of the Aztec Empire, efforts to control flooding in the lacustrine flatlands led to progressive drainage of the lake through canals and dikes. In 1900, the valley of Mexico was entirely drained artificially by the means of a 40 km-long canal to the Northeast of the basin and a tunnel through the mountains. Nowadays, sewage and stormwater are pumped out of the basin through a large canal and tunnel system, while 30% of the city's drinking water is imported through a similar network. The remaining

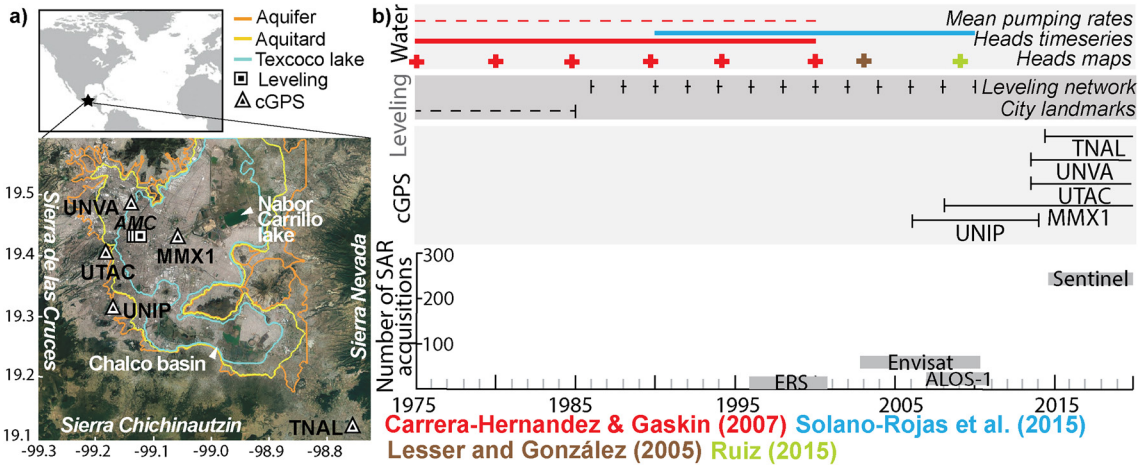

Figure 1. (a) Locations of the continuous GPS data (cGPS) sites (triangles) and of the historical leveling sites (rectangles) on Landsat optical satellite data of the Zona Metropolitana del Valle de México (ZMVM). The extent of the former Texcoco lake before drainage is shown with a cyan contour (Niederberger, 1987) and the extents of the aquifer and aquitard are shown in orange and yellow, respectively (Gobierno del Distrito Federal, 2004). (b) 1975–2020 available data used in this work. Bottom: number and temporal coverage of freely available SAR data acquisitions. Above: openly available cGPS data (locations shown in a), leveling data, and water data. Leveling data exist since 1900 from city landmark measurements (dash-black line) replaced after 1985 by leveling network surveys (black crosses) (Mazari & Alberro, 1991; Sistema de Aguas de la Ciudad de Mexico, 2012). Water data from published works (references shown at the bottom of panel b) exist in the form of water head maps (crosses), timeseries (full lines), and pumping rates (dash lines), color-coded by published work.

70% of the city's drinking water comes from groundwater extraction from wells located throughout the basin with an average depth of 600 m and a maximum depth of 3,000 m. The overexploitation of the aquifer system is causing severe land subsidence in the ZMVM, which has been recognized since the early 1900s (Gayol, 1929). Subsidence exacerbates the risk of flooding and damages both the water distribution infrastructure and sewage networks, causing leakage and contamination. As a result, access to drinking water is a major factor in urban segregation of wealth and results in substandard living conditions.

Previous works have focused on hydrodynamics (e.g., Calderhead et al., 2011; Rudolph et al., 2006), hydrochemistry (e.g., Esteller & Andreu, 2005; Esteller et al., 2012), hazard zonation (Fernandez-Torres et al., 2020), groundwater vulnerability (Hernández-Espriú et al., 2014), groundwater depletion (e.g., Calderhead et al., 2012a, 2012b; Davila-Hernandez et al., 2014), and the related subsidence in the ZMVM and beyond (e.g., Cabral-Cano et al., 2008; Castellazzi et al., 2017; Chaussard, Wdowinski, et al., 2014). Here, we push the limits of application of space geodesy with an across-field data integration in the ZMVM to improve our understanding of the processes controlling land subsidence and of its societal impacts. In particular, we investigate the potential for the existence of elastic deformation and revisit the traditional assumption that subsidence rates are directly reflecting the locations and volumes of groundwater extraction.

1.1. Stratigraphy of the Mexico Valley

Although only very small sections of the former Texcoco lake remain, a large sector of the ZMVM rests on the lake bed's clay-rich quaternary deposits, which constitutes the upper aquitard, initially heavily saturated with salt-rich porewater. This upper aquitard is up to ~100 m thick (Gobierno del Distrito Federal, 2004) (location shown in Figure 1a) and overlies a thick sequence of alluvial-pyroclastic sediments forming a highly productive semiconfined upper aquifer (Ortega-Guerrero et al., 1993). Between 400 and 800 m deep, another portion of the aquifer exists, the lower aquifer, where water is nowadays captured from (Birkle et al., 1995; Morales-Casique et al., 2018). The upper and lower aquifers are separated by the lower aquitard with a maximum thickness of 300 m, composed of Pliocene lacustrine deposits interbedded with basaltic lavas (Mooser et al., 1996). Given the age and lithostatic load experienced by the lower aquitard, the transmissivity and hydraulic conductivity of those clays are significantly lower than those of the upper aquitard. Below the lower aquifer, limestones of the Morelos formation up to 1,500 m thick constitute the mid-Cretaceous basement with a high permeability due to intense fracturing and widespread dissolution channels (Morales-Casique et al., 2018).

1.2. Groundwater in the ZMVM

Over 680 registered wells are operational in CDMX and close to 1,500 registered wells operate in the ZMVM, ranging from 100 to 3,000 m depth (CONAGUA, 2009). For decades, yearly withdrawal rates from the aquifer (45–54 m^3/s) have significantly exceeded natural recharge (20 m^3/s) (CONAGUA 2009), leading to over-exploitation and causing a gradual potentiometric drawdown of about 1.0–1.5 m per year (Lesser y Asociados 2003; Tortajada, 2006a). Prior to the extensive extraction of groundwater, upward hydraulic gradients persisted across the Valley of Mexico (Durazo & Farvolden, 1989; Ortega & Farvolden, 1989) with flowing artesian conditions prevailing. In contrast, the groundwater nowadays flows downwards above the lowered potentiometric level (Huizar-Alvarez et al., 2004), potentially leading to the input of chloride and other chemical constituents to the productive aquifer.

1.3. History of Land Subsidence in the ZMVM

Lowering of the water levels in the aquifer reduces the interstitial water pressure at the base of the aquitard and diffusion of the negative pore pressure anomaly within the aquitard leads to its compaction, causing surface subsidence (Freeze & Cherry, 1979; Santoyo et al., 2005). While drilling for groundwater started in the 1850s, Gayol (1929) provided the first reference of subsidence in the ZMVM, followed by works by Cuevas (1936) and Carrillo (1948). The subsidence history in the city center is well documented and marked by three distinct periods: (1) subsidence at 8 cm/year between 1935 and 1948; (2) subsidence at 29 cm/year between 1947 and 1958 due to the dewatering of aquitards; and (3) subsidence at 5–9 cm/year post-1959, reflecting capping of the wells in the city center directly draining the upper aquitard (Figueroa-Vega, 1984; Ortega-Guerrero et al., 1993) (See Figure 2e). Between 1940 and 1985, up to 7.5 m of land subsidence and a 32 m drop of the potentiometric surface were observed (Ortega & Farvolden, 1989). In the past 20 years, the improved spatial and temporal resolution of subsidence detection has revealed consistent rates up to 35–40 cm/year east of the city's historic downtown and subsidence rates that are highly spatially variable.

1.4. Subsidence Processes

Elastic (reversible) and inelastic (permanent) processes often occur at the same place at the same time linked to groundwater extraction (Poland & Ireland, 1988). Inelastic ground deformation occurs when water heads drop below the previous lowest level leading to grain rearrangement in aquitards (Poland & Ireland, 1988; Wilson & Gorelick, 1996). When the stress exceeds the preconsolidation stress, even if groundwater levels are not lowered to depths greater than the aquitard thickness, the decrease in interstitial porewater pressure leads clay sheets to collapse (Santoyo et al., 2005). Once the clays have been drained, they can shrink down to 30% of their original volume (Alberto-Jaime & Méndez-Sánchez, 2010). While the hydraulic conductivity of aquifers is large enough that they adjust nearly instantaneously to head changes, aquitards have a much lower hydraulic conductivity, resulting in a slow equilibration to heads fluctuations, leading to continued compaction even if water levels are stabilized (Chaussard, Wdowinski, et al., 2014). If all of the ZMVM were built on clays of uniform thickness, the city would subside homogeneously. However, as the city is underlain by lacustrine deposits of variable thicknesses interbedded with volcanic deposits that subsides unevenly, especially on the edges of the former lacustrine system and around isolated volcanic structures withing the valley, the area experiences strong deformation gradients. These gradients are associated with the development of swaths of intense surface fracturing, which damage urban structures including historical buildings and critical urban infrastructures such as water supply and sewage pipes systems and natural gas infrastructure (Cabral-Cano et al., 2010, 2015; Cigna et al., 2011; Santoyo et al., 2005).

1.5. Previous InSAR Surveys

InSAR (Interferometric Synthetic Aperture Radar) is the state-of-the-art method for measuring ground deformation with a high resolution (10–30 m pixel for current operational spaceborne SAR missions) over vast areas (hundreds to thousands of square kilometers) with high precision (up to mm/year). Displacement in the radar line-of-sight (LOS) direction of a SAR satellite is estimated by interfering the phase signal from passes of the same SAR satellite over an area at different times (Bürgmann et al., 2000). Deformation in aquifer systems worldwide has been used to (1) constrain subsiding areas, (2) define aquifer system properties,

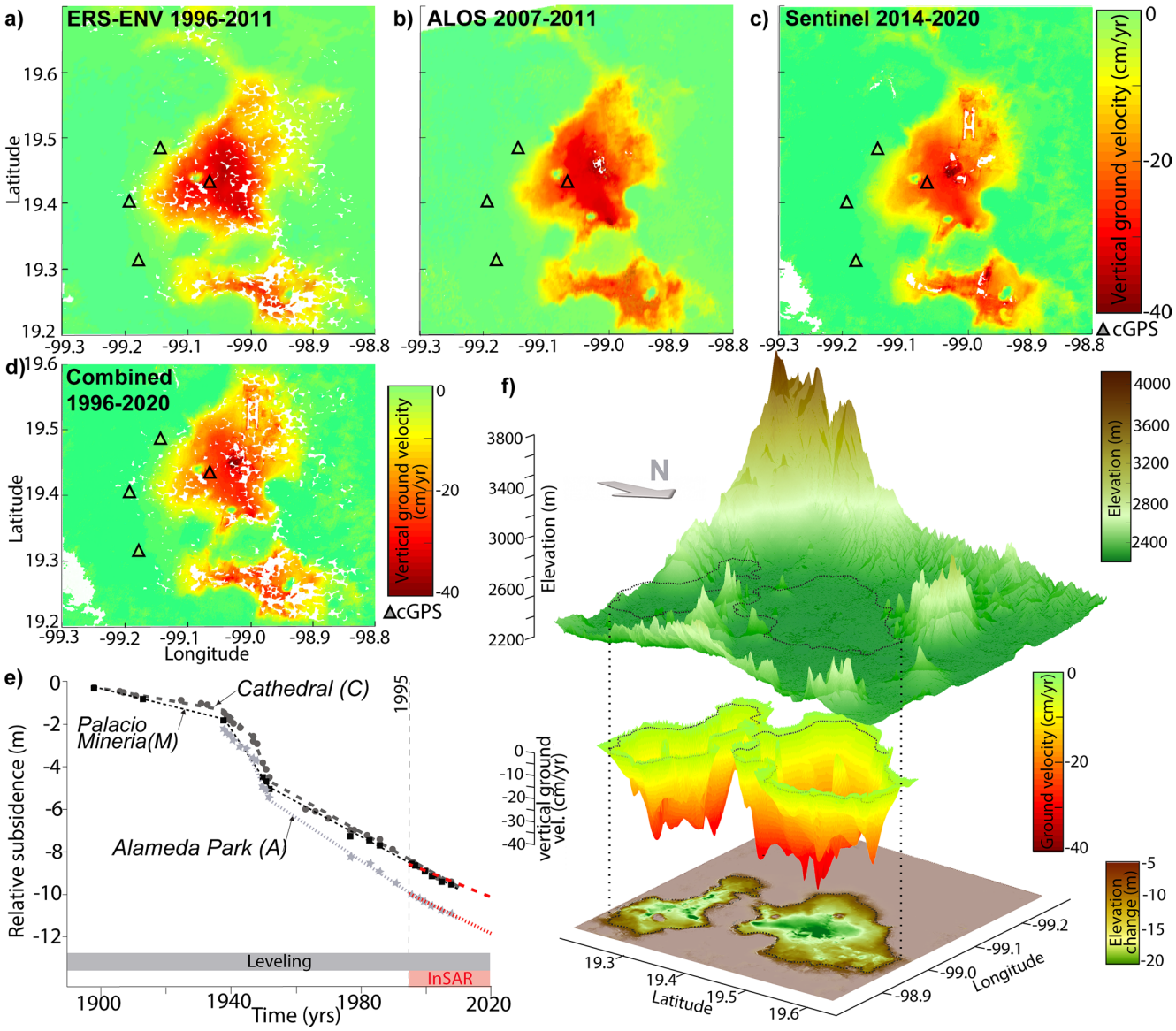

Figure 2. (a–c) Mean vertical ground velocity map from each satellite platform using a correlation-based timeseries approach: (a) European Remote Sensing (ERS)-Envisat, (b) Advanced Land Observing Satellite (ALOS)-1, (c) Sentinel-1. (d) Combined 1996–2020 mean vertical velocity map. (e) Comparison between leveling and Interferometric Synthetic Aperture Radar (InSAR) subsidence rates for city landmarks (locations shown on Figure 1a) (data from Mazari & Alberro, 1991 and Sistema de Aguas de la Ciudad de Mexico, 2012). (f) 3D view of the ZMVM. The contour of the rapidly subsiding areas (>10 cm/year) is shown with a black dashed line on the topography and the interpolated 3D InSAR combined vertical velocity map is shown underneath. The bottom panel highlights the cumulative elevation change since 1950 considering linear subsidence rates.

and (3) improve management practices (Amelung et al., 1999; Bell et al., 2008; Chaussard et al., 2013, 2017; Chaussard, Bürgmann, et al., 2014; Chaussard, Wdowinski, et al., 2014; Miller & Shirzaei, 2015; Motagh et al., 2008). In the ZMVM, Strozzi and Wegmuller (1999) used 1996–1997 SAR data from the European Remote Sensing (ERS) satellites to isolate 30 cm/year of subsidence. Cabral-Cano et al. (2008) combined SAR data from the ERS and Envisat satellites with GPS data and found up to 35 cm/year of subsidence between 1996 and 2005. López-Quiroz et al. (2009) used 2002–2007 Envisat data and found 38 cm/year of subsidence and Osmanoglu et al. (2011) found similar rates when combining Envisat data with GPS data. Chaussard, Wdowinski et al. (2014) used data from the Advanced Land Observing Satellite (ALOS)-1 satellite between 2007 and 2011 and also found subsidence rates of ~35 cm/year. Samsonov and d'Oreye (2017) used 2008–2012 ascending and descending data from the RADARSAT-2 satellite and found vertical subsidence rates of 35 cm/year and horizontal motion up to 5 cm/year. Castellazzi et al. (2017) combined Envisat, Radarsat-2,

and Sentinel-1 data and found similar rates between 2003 and 2016 and Du et al. (2019) used multiple sensors to derive an accumulated 2004–2017 subsidence map. Cigna and Tapete (2021) used 2014–2020 Sentinel-1 data and found subsidence rates up to 39 cm/yr. Solano-Rojas, Wdowinski, et al. (2020) considered various post processing techniques to derive deformation gradients, while Fernandez et al. (2020) generated subsidence risk and angular distortion structural vulnerability maps. Finally, Solano-Rojas, Cabral-Cano, et al. (2020), documented subsidence acceleration in the ZMVM following the September 2017 Puebla and Tehuantepec earthquakes. In this work, we combine all the freely available InSAR data (1996–2020) with continuous GPS data (cGPS), leveling data, water data (well locations, pumping rates, water levels through time), sediments thicknesses data (upper aquitard and aquifer), land use data, and population density data, to reconstruct the subsidence history of the past century in the ZMVM and improve our understanding of (1) the processes controlling the land subsidence rates and spatial extent, and (2) how subsidence relates to the socioeconomic landscape.

2. Methods and Data

To investigate whether subsidence rates and extent are controlled by groundwater extraction locations and volumes in the ZMVM, as generally assumed, we rely on the integration of data from four fields (Figure 1b): stratigraphy (aquifer and aquitard thicknesses), hydrology (well locations, pumping rates, and water levels), geodesy (InSAR, historical leveling, and GPS), and demography (land use type and population density). The timing of existing groundwater and deformation data are shown in Figure 1b. The locations of existing cGPS sites with openly available data and historical leveling sites are shown in Figure 1a, as well as the extents of aquifer and aquitards. Aquitard and aquifer thicknesses used are reported as part of the Technical Standards for Construction in Mexico City (Gobierno de la Ciudad de México, 2019; Gobierno del Distrito Federal, 2004) obtained by interpolating data from deep boreholes, strong motion stations, and microtremor measurements (Auvinet & Juarez, 2002; Perez- Rocha et al., 1995). Groundwater level data are compiled from Carrera-Hernandez and Gaskin (2007), Lesser and Gonzalez-Posadas (2005), and Ruiz (2015), and well locations and pumping rates are taken from Carrera-Hernandez and Gaskin (2007). We used land use data from the "Centro de Investigación en Ciencias de Información Geoespacial" (CONACYT, 2020) and population density data from the "Facebook Connectivity Lab and Center for International Earth Science Information Network - CIESIN - Columbia University (2016)." First, we introduce the InSAR processing method and the approaches used to evaluate the potential existence of elastic deformation. Second, we discuss the ground deformation results combined with analysis of all datasets mentioned above in the Results section.

2.1. InSAR

For data from the ALOS-1 and the Sentinel-1 satellites, we use the ISCE software to produce interferograms coregistered to a reference image (Fattahi et al., 2017; Rosen et al., 2015), while for data from the ERS and Envisat satellites, we use the GMTSAR software (as ISCE does not support ERS and Envisat data). For all interferograms, we remove topographic contributions using the Shuttle Radar Topography Mission (SRTM) 1-arc second digital elevation model, multilook the interferograms to achieve a spatial resolution of ~90 m spacing, and use the statistical-cost network-flow algorithm (SNAPHU) for phase unwrapping (Chen & Zebker, 2002). To track ground deformation between the first and the last SAR acquisitions of each satellite platform, we use the correlation-based timeseries approach (Chaussard et al., 2015a, 2015b) through MintPy (Yunjun et al., 2019) to improve upon the spatial coverage of previous studies, which relied on Small Baseline Subset (SBAS) or Permanent Scatterers (PS) methods. We use the ERA-5 meteorological global atmospheric model to correct the tropospheric delay (Jolivet et al., 2014) and remove long-wavelength signal in the form of a ramp to decrease ionospheric delay, residual tropospheric delay, and to remove potential interseismic or postseismic signal (Chaussard et al., 2016). Errors correlated with baselines (digital elevation model [DEM] errors) are removed following the method of Fattahi and Amelung (2013), the Root Mean Square (RMS) of residual phase time-series for each acquisition is calculated following Yunjun et al. (2019), and unwrapping errors are identified using the phase closure technique and manually corrected as needed.

For each satellite platform, the InSAR timeseries analysis provides a mean LOS velocity map and a time-series at each pixel that maintains similar ground characteristics between successive passes (temporal

coherence >0.7). The ERS and Envisat data are processed together into timeseries (Chaussard, Bürgmann, Fattahi, Johnson, et al., 2015), while the ALOS-1 and Sentinel-1 data are processed individually. We assume that the horizontal component of deformation is negligible and convert LOS motion (dLOS) into vertical displacement (dv) relying on the mean incidence angle θ of each satellite ($dv = dLOS/\cos\theta$). This assumption is justified by previous works (e.g., Osmanoglu et al., 2011 and Samsonov & d'Oreye, 2017) which showed that the horizontal motion is small compared to the vertical motion (<5 cm/year), in agreement with our observations that the differences between the projected vertical rates of various time periods are <5 cm/year (Figure S1c–S1e).

The good agreement between the ALOS-1 and Sentinel-1 vertical velocity maps (Figures 2b, 2c, and S1e), which do not overlap temporally, suggests that subsidence rates are mostly constant. Openly accessible GPS data from the TLALOCNet (Cabral-Cano et al., 2018), UNAVCO, and NOAA-NGS archives and their solutions from Blewitt et al. (2018) (Figure S2) confirm that subsidence rates have been mostly constant since 1996. Based on the constant rates seen by individual SAR satellites, cGPS stations, and on the agreement between InSAR and leveling rates, we combine the individual satellite timeseries into a single timeseries to constrain the 1996–2020 mean vertical deformation. To do so, we (1) reference each timeseries to the same pixel, (2) convert each timeseries to vertical using the respective satellite geometries, (3) resample each timeseries to a similar geocoded grid, and (4) apply pixelwise offsets equivalent to fitting a linear slope plus an offset to timeseries of each pixel (Figure S1a). The ALOS-1 timeseries is offset to match the ERS-Envisat timeseries in their period of overlap as Figures 2a and 2b confirm that similar deformation rates are observed by both platforms. The ERS-Envisat-ALOS-1 timeseries is linked to the Sentinel-1 timeseries by computing pixelwise offsets based on (1) the temporal gap between the last ALOS-1 date and the first Sentinel-1 date, and (2) the mean vertical displacement rate from the Sentinel-1 timeseries, which has more acquisitions than the ERS-Envisat-ALOS-1 timeseries (Figure S1a). The resulting 1996–2020 mean vertical velocity map is shown in Figure 2d.

2.2. Method for Isolating Potential Elastic Deformation

To evaluate whether a portion of the observed InSAR deformation is reversible, we follow the method of Chaussard and Farr (2019) and apply an Independent Component Analysis (ICA) to separate independent sources mixed in the deformation signal relying on the FastICA algorithm (Hyvärinen & Oja, 1997). ICA is a computational method in which statistical independence is used to isolate different time-dependent surface displacement histories into independent components (ICs) with distinct spatial (scores) and temporal (eigenvalue timeseries) patterns (Chaussard et al., 2017; Gualandi et al., 2017). The number of ICs to retain, which reflects the number of deformation patterns with different spatio-temporal properties when ignoring the noise, is selected based on the percentage of nonzero eigenvalues retained. As the temporal sampling of older platforms (ERS, Envisat, ALOS) does not enable isolating potential short-term deformation (revisit time > 30 days), we apply the ICA to the Sentinel-1 timeseries (up to 6 days repeat).

Results are presented for each component as an eigenvalue timeseries showing the magnitude of the IC contribution at each acquisition (Figure S3b) and a score map showing the pixels experiencing the associated timeseries (Figure S3c). The product of the scaled pixelwise score by the eigenvalue at a given time gives the contribution in terms of deformation units. Our ICA considers 3,724,957 samples (pixels) per epoch and 251 epochs (Sentinel-1 acquisitions). The eigenvalue of one component (IC1) corresponds to 99.3% of the sum of all the nonzero eigenvalues, while a second component retains only 0.2% of the eigenvalues. Thus, only one deformation pattern is significant in the ZMVM and captured by IC1. Similar results are obtained when removing the mean linear trend from the timeseries before performing the ICA (IC1 = 97.2% of nonzero eigenvalues retained; IC2 = 0.6%) and in a Principal Component Analysis (PC1 explains 97.2% of the variance, PC2 explains only 0.7%). ICA results are discussed in Section 3.1.

3. Results

3.1. Rapid, Constant Subsidence Since 1950

Figures 2a–2c shows the InSAR mean vertical velocities individually processed with the correlation-based method for the four satellite platforms (ERS, Envisat, ALOS-1, Sentinel-1), covering 1996–2020. The

deformation spatial extent and the amplitude are similar, confirming continuous, rapid subsidence east of the city's historic downtown (location of the leveling sites, Figure 1a). The maximum observed vertical subsidence is 50 cm/year at 19.445 N and −99.032 E (Figure S4), just west of the Nabor Carrillo lake (location shown on Figures 1a and S4). This area remains coherent only in the Sentinel-1 mean velocity map, which has the shortest repeat time (Figure 2c). This rate is greater than the maximum rates observed by previous works of 35–40 cm/year, as the area experiencing this very rapid subsidence used to be decorrelated in previous SBAS and PS analyses. In contrast, a correlation-based timeseries of the 12 to 6 days repeat Sentinel-1 data enables retrieving the rapid deformation in this area which was partially drained in 2015 as part of the construction effort for the new airport (which was later abandoned) (Figure S4). Areas that are in common with previous works show similar subsidence rates (Figures 2a–2d). Another feature of the ZMVM subsidence is the existence of high deformation gradients. Subsidence rates greater than 10 cm/year are observed less than 200 m from stable, nonsubsiding areas (Figures 2a–2c, and 2f). Contours of the two areas showing subsidence rates greater than 10 cm/year are shown with a black dash line on Figure 2f (and in Figures 4 and 5 and Figures S1, S3–S6, and S8, S9). It is clear that the extent of the subsiding areas is positively correlated with the extent of former lake Texcoco and with the extent of the quaternary upper aquitard (Figure 1a). Gradients will be further explored in Section 4.2 in the context of mapped fractures in the socioeconomic landscape.

The four satellite platforms have different incidence angles and thus different sensitivity to horizontal deformation; the general agreement between the individual mean vertical velocity maps projected using the nominal satellites incidence angles, further confirms that most of the InSAR recorded deformation is vertical. In Figures 2a–2d, the cGPS stations linear vertical deformations are color coded similarly to the InSAR vertical velocity and show a complete agreement. Time series at the InSAR pixel location of the station MMX1, located in the subsiding area, is compared to the GPS vertical displacement component in Figure S2. When considering the entire time span, the best fit linear regression to the MXX1 vertical deformation is a rate of 27 cm/year of subsidence, compared to a rate of 26 cm/year in the combined vertical InSAR timeseries. Analysis of the residuals from the linear fit to the vertical deformation of MMX1 reveals a continuous positive trend at 5 mm/year, with the exception of a 19 months period following the September 19, 2017 earthquake (Figure S2b). When considering the MMX1 deformation only prior to the earthquake, a similar slope is observed in the InSAR and GPS vertical deformation. This agreement across datasets is consistent with previous, shorter term studies (Cabral-Cano et al., 2008; López-Quiroz et al., 2009; Osmanoglu et al., 2011). Additionally, as previously suggested by Osmanoglu et al. (2011), small differences may exist between InSAR and GPS (<1 cm/year) data due to the variability of subsidence rates over short distances sampled by InSAR, the inherently discrete nature of GPS measurements, and the different spatial resolution and noise of each technique. The GPS residuals from linear regressions are further evaluated in the context of short-term (seasonal) changes in the next section.

The comparison between the leveling data and the InSAR data shows a good agreement at the locations of city landmarks within the historic city center (Figure 2e). In addition, the leveling data shows that constant rates of subsidence have been observed since the 1950s after water wells within the city center were closed and water wells were moved to the then outskirts of the city. Based on the constant rates seen by individual SAR satellites, cGPS stations, and the agreement between InSAR and leveling rates, we assume linear subsidence rates between 1950 and 2020, acknowledging that very localized nonlinear deformation may exist, and derive the cumulative elevation loss (Figure 2f), which reveals up to 38.7 m of elevation loss and many areas with over 20 m elevation loss. In systems controlled by groundwater pumping, elastic deformation may be masked by the long-term continuous deformation (Chaussard & Farr, 2019). We investigate the potential existence of such elastic deformation in the ZMVM in the next section.

3.2. Absence of "Hidden" Short-Term Elastic Deformation

Short-term (seasonal) deformation deviating from a linear trend would suggests that the compacting aquifer system has the potential to recover storage capability under proper management (Amelung et al., 1999; Freeze & Cherry, 1979; Terzaghi, 1996). Here, we investigate the potential existence of such short-term deformation "hidden" within the rapid long-term subsidence with (1) the ICA method (Chaussard & Farr, 2019) applied to the 2014–2020 Sentinel-1 data, and (2) analysis of the 2004–2020 cGPS data.

The ICA shows that only one component of deformation is present in the ZMVM, with the magnitude of IC1 representing 99.3% of the sum of all nonzero eigenvalues (Figure S3a). A second component is evaluated to ensure that no signal is missed (Figure S3b and S3c), but as only 0.2% of the eigenvalues is retained by IC2, this component is not significant. The IC1 eigenvalue timeseries reveals a linear signal with a strong negative slope (Figure S3b, black), and the IC1 score map (Figure S3c top) shows positive values in the subsiding areas identified in the mean vertical velocity maps of Figure 2. IC1 thus captures the continuous rapid subsidence affecting the areas highlighted by the mean vertical velocity maps (Figure 2). In contrast, the IC2 eigenvalue timeseries reveals a small positive slope between 2014 and 2017 (when Sentinel-1 acquisitions were every 12 days), leveling to a negligible slope post-2016 (6 days repeat) and yearly "jumps" corresponding to changes in perpendicular baselines. The IC2 score is dominated by a long-wavelength signal to the West and South with positive score values (yellow to orange colors) in the southwest corner (Figure S3c). This suggests that IC2 captures noise embedded in InSAR timeseries and confirms that one component of deformation dominates in the ZMVM: long-term, rapid, constant subsidence. Localized short-term nonlinear deformation may exist, as captured by small "blobs" in the IC2 score map, but is very minor.

The absence of a significant short-term time-varying signal in the ICA shows that no major elastic (reversible) deformation is taking place in the ZMVM. This is in contrast to observations made in other fast subsiding environments such as the (clastic-prevalent) Central Valley and the Silicon Valley aquifers, in California, USA, where in both cases, ICA isolated short-term elastic deformation embedded in the longer-term deformation (Chaussard, Bürgmann, et al., 2014; Chaussard & Farr, 2019; Chaussard et al., 2017). The lack of significant short-term, seasonal or semi-annual deformation, in the ZMVM confirms negligible recharge compared to withdrawal and implies that continuous inelastic (irreversible) degradation of the aquifer-aquitard system underlying the ZMVM is taking place.

We additionally investigate the potential for short-term deformation in the cGPS vertical deformation signal by removing the long-term trend (Figure S2). At first glance, the vertical GPS displacement residuals suggest seasonal deformation (Figure S2). However, this seasonality is observed for all stations regardless of their locations on soft or hard rocks, suggesting that it may be a common-mode signal with a regional (long wavelength) footprint associated with tidal loading, surface water loading, or tectonic loading that are independent of the local hydrologic processes. To focus on local hydrologically induced deformation, we remove such common-mode signals using a nearby station on stable ground. We use the TNAL station on the Sierra Nevada as it shows no clear vertical deformation. Comparable results were obtained using UXAL, a station located further East in Xalapa, Veracruz. The common-mode-reduced GPS residuals, which capture all the local signal deviating from a linear trend, are shown in Figure S2b and S2c. No clear seasonal deformation is observed at the stations located in the ZMVM both inside (MMX1) and outside (UNIP) of the subsiding areas. These observations are consistent with the InSAR analysis and with previous works that similarly did not detect noticeable seasonal fluctuations (Osmanoglu et al., 2011). The absence of a seasonal component in the cGPS data confirms that (1) the great majority of the deformation observed is irreversible and (2) nonlinear deformation, if present, it is only highly localized, supporting the InSAR-ICA results.

Analysis of the residuals from a linear fit at MMX1 reveals an increase of 3.5 cm/year of the subsidence rate compared to the background rate for a period of 19 months following the September 19, 2017 Mw7.1 earthquake, which caused strong ground motion in the ZMVM (Sahakian et al., 2018) (observed both in the raw residuals and the common-mode reduced residuals, Figure S2b). Greater subsidence after this earthquake, also detected by Solano-Rojas, Cabral-Cano, et al. (2020), suggests a decrease in near-surface rigidity due to grain rearrangement allowing sediments to stretch more easily. Similar observations of the effect of strong ground motion on near-surface rigidity were made by Viens et al. (2018) after the 2011 Mw 9.0 Tohoku-Oki earthquake, where a decrease in seismic velocity was observed in the Tokyo area. There, a logarithmic recovery over various timescales was modeled with a viscoelastic rheology to illustrate the medium returning to its pre-event state. In the ZMVM, the effect of the strong ground motion from the earthquake is seen for 19 months (until April 2019) but further analysis is beyond the scope of this work and will be addressed through future work combining geodetic and seismic noise analyses.

3.3. Controls on Subsidence Rates and Spatial Extent

We reevaluate the traditional assumption that subsidence rates and extent are directly controlled by groundwater extraction locations and volumes. To do so, we use a three-pronged approach. First, we compare the spatial extent of ground deformation to groundwater levels evolution through time and to pumping rates. Second, we use a multivariable analysis integrating all available datasets (Section 2), and finally, we employ a Gaussian Process Regression (GPR) (a nonparametric, Bayesian machine learning approach) to quantify how well subsidence rates can be predicted by combined and independent datasets (water levels, pumping rates, aquifer thickness, aquitard thickness, population density, and land use type).

Figure S5 shows stepwise 5 years differences in potentiometric surfaces in the ZMVM between 1975 and 2000 (Figure S5a–S5e; Carrera-Hernández & Gaskin, 2007), for 2000–2003 (Figure S5f; Lesser & González-Posadas, 2005), and for 2003–2009 (Figure S5g, Ruiz, 2015). While lowering of groundwater levels is occurring in the subsiding areas (black dash line), the greatest lowering is observed outside of the subsiding areas, suggesting that water level fluctuations and subsidence are concurrent processes but may not have a direct or causal relationship, or alternatively that potentiometer surface sampling is either spatially biased or insufficient.

Figure S5i shows that the great majority of wells are located outside of the subsiding areas as a consequence of the 1950 decision to migrate production wells outside of CDMX. Therefore, no obvious spatial correlation is detected between subsidence rates and well locations. Hernández-Espriú et al. (2014) and Solano Rojas et al. (2015) similarly suggested that ground deformation rates cannot be correlated solely with groundwater pumping intensity because of existing subsurface stratigraphic heterogeneities.

We find that between 1975 and 2009 the average water level decrease is approximately constant at 1–1.5 m/year, in agreement with Carrera-Hernández and Gaskin (2007) who reported drawdown rates around 1 m/year (and up to 2.5 m/year in some areas), Ortega-Guerrero et al. (1993) and Ortiz Zamora and Ortega Guerrero (2010) who reported drawdown rates of 1–1.5 m/year, and Hernández-Espriú et al. (2017) who reported regional water level drop on the order of 0.5–2 m/year. Based on the linear groundwater levels evolution, confirmed by the groundwater time series of Solano Rojas et al. (2015), we extrapolate the 1975–2009 data to estimate 1950–2020 lowering of water levels (Figure S5h). We acknowledge that this linear temporal interpolation of groundwater levels throughout the ZMVM is a simplification, as specific wells may experience more complex fluctuations. However, published local water levels timeseries confirm linear fluctuations (Solano-Rojas et al., 2015), and the lack of systematic water levels reporting prevents us from developing a more complex model. We find that in these past 70 years, the net water level lowering is on average 107 m, while the total volume of groundwater extracted is 65–70 km^3 (Figure S5h). This estimate is on the higher end of the volume calculated using the reported water extraction from registered wells of 65 km^3, considering extraction rates of 5 m^3/s between 1950 and 1960, 8.5 m^3/s between 1960 and 1970, 16 m^3/s between 1970 and 1980, 27 m^3/s between 1980 and 1990, 45 m^3/s between 1990 and 2000, 50 m^3/s between 2000 and 2010, and 55 m^3/s since 2010 (CONAGUA, 2009; Del Campo et al., 2014; Mejía et al., 2007; Ruiz, 2015). The existence of clandestine water wells in the ZMVM is likely accounting for the fact that the total extracted volume calculated from water level changes is on the higher end of the volume calculated using reported pumping volumes.

To constrain the controls on subsidence rates and spatial extent, we perform a multiparameter analysis and evaluate potential relationships between pixelwise subsidence rates and the following datasets: water head changes over a similar timespan, pumping rates, aquifer thickness, aquitard thickness, population density, and land use type (Figure 3). We use a multilinear regression (MLR) analysis, which has been shown to enable isolating the causes of land subsidence (Abdollahi et al., 2019; Tien Bui et al., 2018). The MLR analysis confirms the absence of relationships between subsidence rates and water head changes or pumping rates (Figures 3c and 3e). Similarly, no relationship is observed between subsidence rates and land use type or population density (Figures 3d and 3f; see Figure S6 for the datasets), which is understandable given the locations of water extraction wells. In contrast, the aquifer and aquitard thicknesses (which have similar spatial attributes) show strong correlations with subsidence rates ($R^2 = 0.80$; Figures 3b and 3a). The aquitard thickness to subsidence rates relationship has a lower deviation (0.008) and a lower mean square error (0.0005) than the aquifer thickness to subsidence rates relationship (0.011 and 0.0007) (Table S1).

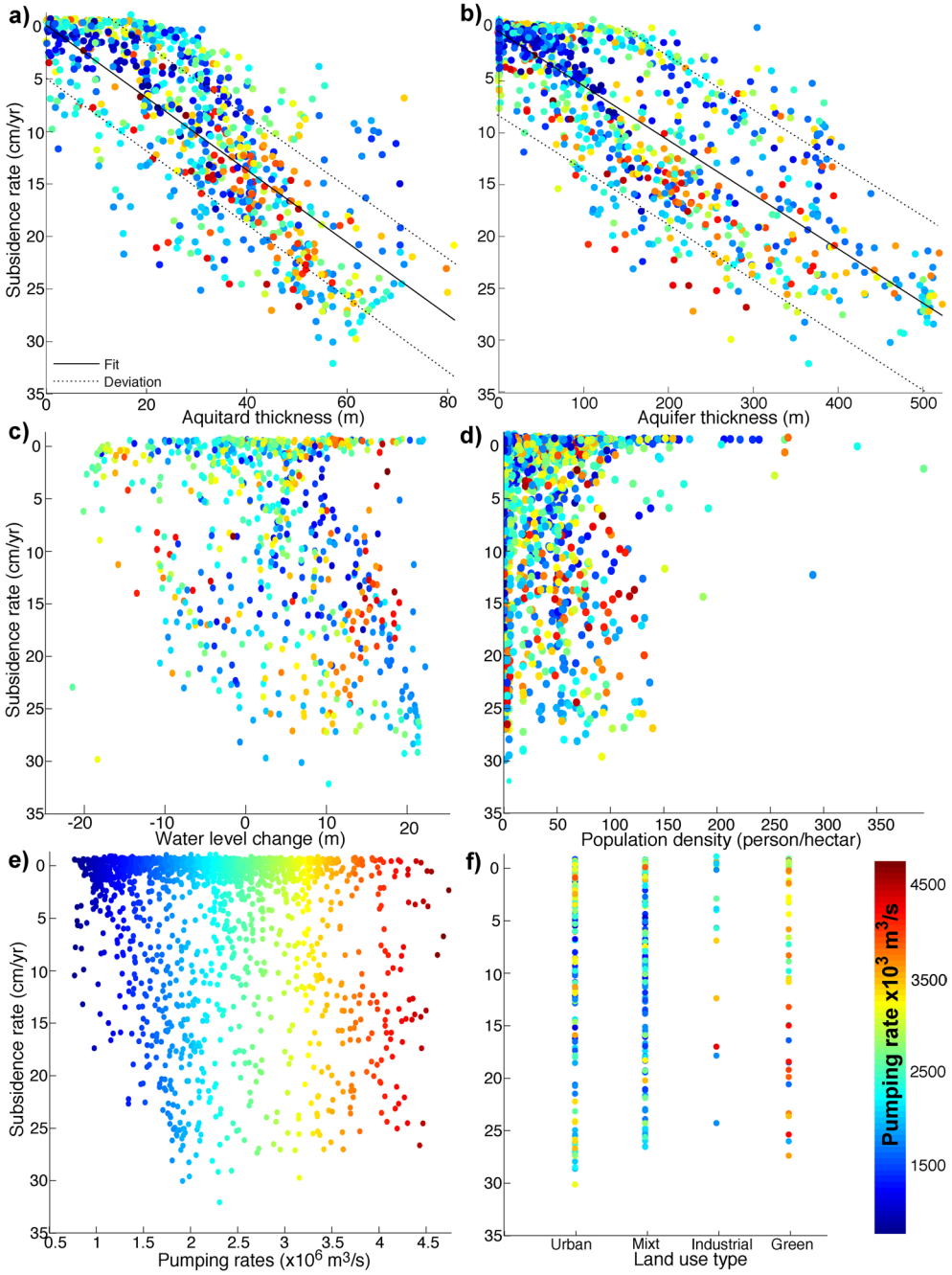

Figure 3. Multilinear regression (MLR) analysis (data color coded by pumping rates) evaluating potential relationships between pixelwise subsidence rates and: (a) aquitard thickness; (b) aquifer thickness; (c) water head changes; (d) population density; (e) pumping rates, and (f) land use type.

This linear relationship between subsidence rates and aquitard thicknesses agrees with observations of Cabral-Cano et al. (2008) who correlated subsidence rates with the lacustrine clay thickness derived from seismic imaging and Solano Rojas et al. (2015) who relied on a subset of subsidence rates. Our analysis thus suggests that for every additional meter of clay thickness the subsidence rate increases by 3 mm/year (slope value).

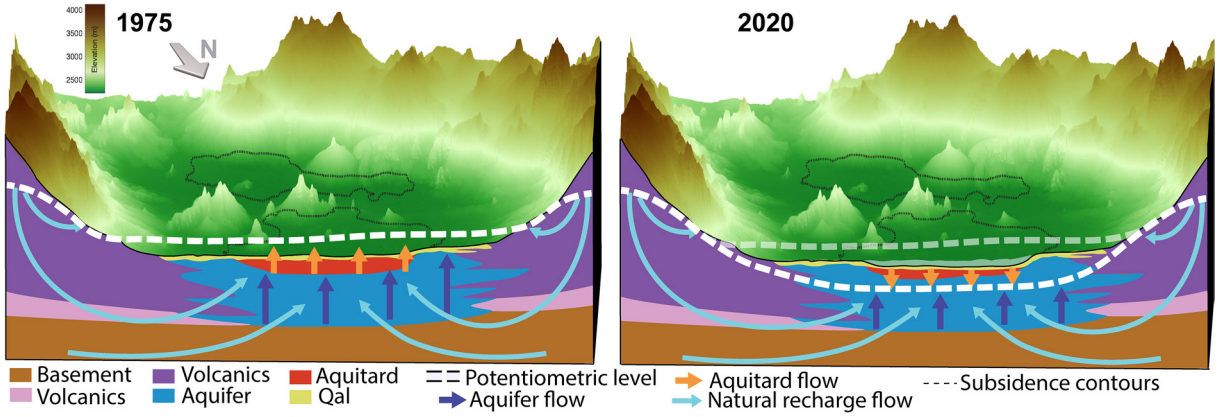

Figure 4. Schematic representation of the water flow in the Zona Metropolitana del Valle de México (ZMVM) in 1975 (left) and in 2020 (right). (Left) Upward flow persisted across the basin floor prior to the decades of significant groundwater extraction due to recharge and infiltration from mountain runoff on the edge of the basin leading to artesian conditions. (Right) In contrast, the decades of groundwater extraction have mostly lowered the potentiometric level to a level deeper than the base of the upper aquitard (Figure S9), leading to downward flow of polluted water from the aquitard into the producing aquifer.

3.4. Future Deformation Forecast

We further demonstrate the validity of our MLR results by employing a GPR approach, a nonparametric, Bayesian machine learning approach. This method builds upon the MLR by considering linear and non-linear relationships between multiple dependent parameters. We train the data on the various parameters (as combinations and independently) and predict the subsidence rates (Table S1; Figure S7). In agreement with the MLR results, comparable R^2 (0.8) are obtained with the GPR approach when considering the aquitard and aquifer thicknesses as individual predictors, but a lower deviation is obtained when using the aquitard thickness to predict the subsidence rates (Figure S7). In addition, considering more variables than the aquitard thickness does not improve the prediction accuracy (Table S1). The GPR analysis also shows that the data do not warrant a more complex relationship than a linear regression between subsidence rates and aquitard thickness. The complexity added by a power fit law used by Cigna and Tapete (2021) leads a greater

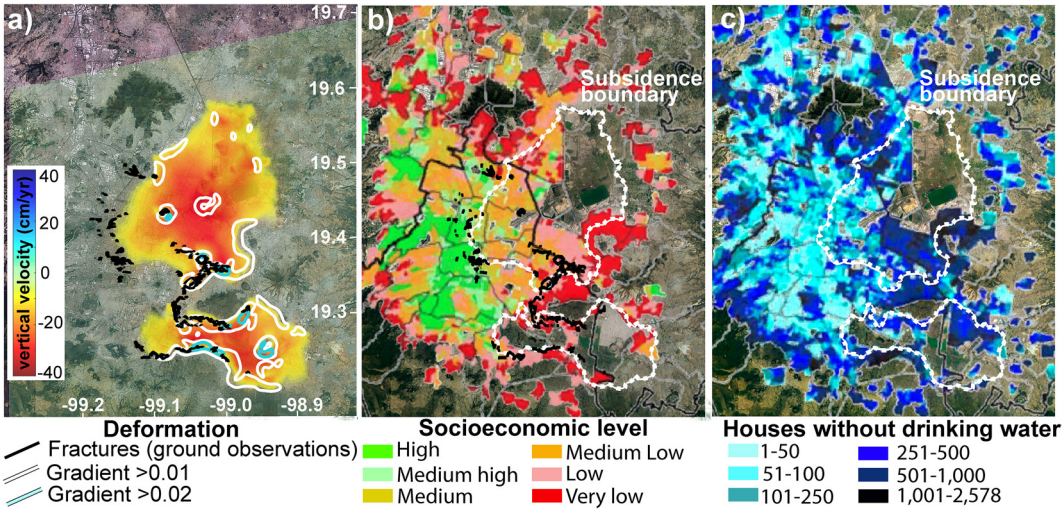

Figure 5. (a) gradient of the mean vertical deformation (white and cyan contours) compared to the locations of mapped fractures and fissures (black, data from Carreón-Freyre et al., 2017), overlaying the interpolated Interferometric Synthetic Aperture Radar (InSAR) mean velocity maps shown in transparency over a Landsat image of the Zona Metropolitana del Valle de México (ZMVM). (b) and (c) Extent of the subsiding areas (white contour) in a social context: (b) socioeconomic levels (data from Tortajada, 2006a), (c) houses with substandard drinking water supply (data from Tortajada, 2006a).

Akaike information criterion than a linear fit and likely result from their usage of interpolated data, which leads to a biased sampling.

We use the linear relationships observed between subsidence rates and the aquitard thickness to estimate the current level of compaction of the aquitards and forecast the remaining compaction (Figure S8). We find that the aquitards are currently 17% compacted on average, with most values ranging from 15% to 20% compaction (Figure S8f) and that it will take on average ~150 years for the clays to shrink down to 30% of their original volume (Figure S8h; maximum reduction in original clay volume due to drainage in the ZMVM according to Alberto-Jaime & Méndez-Sánchez, 2010), which will lead to an additional subsidence of up to 20 m in the CDMX area and up to 30 m in the Chalco basin (Figure S8d).

4. Discussion

4.1. Changes in Water Flow and Impact on Water Quality

Under natural conditions, groundwater discharge in the basin occurred as springs at the edge of the Valley of Mexico, used as the sources for water in both pre-Hispanic and colonial times by water works such as the Chapultepec aqueduct. Thus, prior to the extensive extraction of groundwater from the semiconfined aquifer, upward flow persisted through the aquifer and aquitard (Durazo & Farvolden, 1989; Ortega & Farvolden, 1989), with artesian conditions prevailing across the basin floor (Figure 4 left). As a result of the upward flow through the aquitard, the bottom of the saline zone had migrated to a level above the base of the aquitard (Huizar-Alvarez et al., 2004; Ortega-Guerrero et al., 1993, 1999) and remained isolated from the aquifer groundwater below. In addition, the aquitard layer was impermeable and thus acted to limit surface pollutants from reaching the underlying aquifer.

Inelastic ground deformation occurs when the stress in the aquifer system exceeds the preconsolidation stress, leading to grain rearrangement in aquitards, even if the groundwater levels are not deeper than the aquitard thickness. However, In the ZMVM, over a hundred years of groundwater extraction have lowered the position of the potentiometric surface to a level close to or below the bottom of the former lake (depending on the thickness of the aquitard) (Figures S9 and 4 right). Hydrologic and sedimentary data show that by 1990, less than 20% of the base aquitard surface area was still 20 m deeper than the groundwater levels, and only 1% was 40 m deeper than the groundwater levels (Figure S9). By 2000, only 15% of the base aquitard surface area was still 20 m deeper than groundwater levels. Considering the linear groundwater levels evolution shown by Solano Rojas et al. (2015), by 2030, the water levels will have dropped below the quasi-entirety of the aquitard thickness.

We expect a delay between the lowering of groundwater levels and aquitards compaction due to the aquitard's low hydraulic conductivity, which results in a slow equilibration relative to heads fluctuations. The continuous linear subsidence thus suggests that compaction of the shallow aquitard layer has not yet "caught-up" with the current and continuously evolving stress in the system. The aquitard is draining naturally at constant rates, resulting in the mostly constant subsidence rates that can be predicted from the aquitard thickness, in contrast to the 1935–1950 period during which pumping was taking place directly within the aquitards, increasing the drainage speed and causing the accelerated subsidence seen in the historic leveling data. The currently observed subsidence rates are expected to persist unless water levels are brought back up, and residual compaction would continue despite potential water level recovery due to the low hydraulic conductivity of clays. Even if groundwater levels were to be raise, there is no hope for recovering the majority of the already-lost elevation and the lost aquitard storage capacity because the inelastic compressibility of clays is 1–3 orders of magnitude greater than their elastic compressibility (Pavelko, 2004; Riley, 1998).

While groundwater levels do not need to be below the base of the aquitard for clays to compact (as diffusion of the negative pore pressure anomaly is transmitted through the system), the depth of water levels relative to the base of the aquitard influences water migration. The large contrast in hydraulic conductivity between the aquifer and the aquitard due to aquifer depressurization results in vertical flow (Neuman & Witherspoon, 1969), and the decline in the potentiometric surface has led to a reversal of the hydraulic gradient (Figure 4 right). Downward flow now dominates through the aquitard, while upward flow remains in the aquifer up to the current potentiometric level (Figure 4 right, Figure S9). Clays from the aquitard are

thus transmitting water vertically through a "drip process" to the underlying aquifer (Cardona & Hernández, 1995). Porewater in the aquitard is saline or worse, contaminated with surface pollutants or organic material from leaky sewage, leading to a mix of salts and chemicals being released from the aquitards to the underlying aquifer and progressively, increasingly impairing the quality of pumped water. In addition, as they shrink, clays fracture, which enables pollutants and sewage water to percolate down from the surface (Castellazzi et al., 2018; Rudolph et al., 1991). Thus, while the lowering of hydraulic heads in the aquifer is not controlling the subsidence rates and extent, it is responsible for inducing the migration of low-quality water from the aquitard to the aquifer, eventually setting the stage for a water pollution crisis.

4.2. Socioeconomic Context: Infrastructure Damage, Poverty Levels, and Water Access

Surface ground faulting and fracturing occur as a result of differential subsidence, causing damage to critical urban infrastructures (Holzer & Johnson, 1985). We calculate the horizontal gradients of vertical subsidence to isolate areas experiencing large differential subsidence (subsidence rates with large changes in amplitude over short spatial distances). Gradient calculations are based on a Sobel gradient operator in which the gradient of a pixel is a weighted sum of pixels in the 3-by-3 neighborhood. The resulting gradient is processed through a gaussian filter to reduce the noise and plotted as contour intervals highlighting a 1:1,000 ratio of mean vertical velocity to horizontal distance, in m/year/km (maximum contours of 0.1 and 0.2). We then compare the InSAR high-gradient locations to mapped fissures and fractures (Figure 5a, Carreón-Freyre et al., 2017). Figure 5a confirms that mapped fractures and fissures (black lines) are located in high gradient areas (white and cyan contours). However, several high gradients areas lack mapped fractures and fissures likely due to: (1) the catalog of fractures and fissures being incomplete and future fieldwork could be guided by this gradient map; (2) some areas having limited urban features, impeding mapping (i.e., in the center of the northern subsiding area near the Nabor Carrillo lake); and (3) in some areas strain is relieved progressively or fractures are repaired.

In the ZMVM, more than 1.1 million houses lack access to safe water and over half a million lack access to adequate sanitation (Tortajada, 2006b, Figure 5c). We qualitatively compare the social landscape to subsiding and high gradient areas in Figures 5b and 5c. High subsidence gradients, which result in damages to buildings and infrastructure, are observed in areas that exhibit low and very low socioeconomic levels (Figure 5b). This spatial-correlation between socioeconomic levels and high deformation gradient areas can be explained by the fact that high- or medium-income inhabitants who live in areas experiencing high differential deformation are more adept to overcome the associated challenges and are thus more resilient; in contrast, low-income and very low-income inhabitants cannot afford to relocate as their real estate value is increasingly depressed by fissuring and fracturing.

In addition, the greatest concentration of houses with substandard access to drinking water is observed within the subsiding areas (Figure 5c). This limited access to water can be explained by the following observations. The subsiding areas are located in the center of the basin (Figure 5a), away from the sources of water recharge (the eastern slope of the Sierra de las Cruces, the northern slope of Sierra de Chichinautzin and the western slope of the Sierra Nevada, locations shown on Figure 1a) and where only a limited number of active water wells exist (Figure S5i). However, to reach this part of the city where no wells exist (Figure S5i), the water distribution system has to cross the boundaries of the subsiding areas and is thus exposed to high deformation gradients. Such deformation gradients are correlated with the occurrence of faulting and fracturing which increases the occurrence of infrastructure damage (Figure 5a). As a result, the water distribution system reaching the rapidly subsiding areas is disproportionally affected by damages, leading to residents experiencing decreased water access and water quality. These observations suggest that the living standards within the ZMVM are in part consequences of the water crisis, and the water crisis further reinforces existing disparities (Fernandez-Torres et al., 2020).

5. Conclusions

Integration of 1900–2010 leveling data with 1996–2020 vertical InSAR ground deformation and 2002–2020 cGPS deformation shows that subsidence rates have been approximately constant at least since 1950 in the ZMVM, when the last profound management decision for local underground water supply to the city took

place. Our correlation-based InSAR time series approach reveals subsidence rates up to 50 cm/year in the northeast sector of the city, in an area that is still not urbanized and where deformation remained undetected due to decorrelation in previous InSAR analyses. The independent component analysis of InSAR data and the determination of the common-mode error in the open source cGPS data reveal that no significant elastic deformation exists in the ZMVM. Integration of hydrologic, stratigraphic, geodetic, and demographic datasets shows that the locations and magnitudes of groundwater extraction cannot uniquely account for the spatial extent and rates of the observed land subsidence. Instead, a strong positive linear relationship between subsidence rates and the thickness of the upper aquitard is isolated. Our data shows that for every additional meter of clay, the subsidence rate increases by 3 mm/year. As of 2020, on average the upper aquitard is 17% compacted and we estimate that under the current conditions it may take ~150 years to reach full compaction, which will lead to additional subsidence up to 30 m. These subsidence rates will persist unless water levels are brought back up to shallow depths. Even if water levels were to be raised, there is no hope for recovering the great majority of the lost elevation and the lost storage capacity of the aquitard.

Since 1950, water wells are located only outside of the confined aquifer, but the lowering in pore pressure is transmitted throughout the valley, resulting in the water levels being now deeper than the majority of the clay thickness. As a consequence, water flow in the aquitard is now downward and, since the aquitard pore water is salted and likely polluted, this gradient reversal leads to a decrease in the aquifer water quality. Finally, areas with high subsidence gradients coincide with a high density of surface faulting and fracturing, which (1) increases percolation of low quality water through the aquifer system, (2) affects the hydraulic infrastructure, and (3) further decreases access to water resources for the population living in the subsiding areas.

These results suggest that subsidence greatly influences the socioeconomic landscape and even the future urban viability of Mexico City. Given that only one-third of water consumption in the ZMVM comes from adjacent basins and runoff and the remaining supply is drawn from its underlying aquifer system, the stage is set for a dual water and subsidence crisis if no drastic water management actions are implemented (such as reusing treated wastewater for groundwater recharge and agricultural and urban-landscape irrigation, e.g., Chelleri et al., 2015; Mazari-Hiriart et al., 2019; National Research Council, 1995).

Data Availability Statement

The ERS and Envisat data used are freely available through the WInSAR repository and the ALOS-1 and Sentinel-1 data through the Alaska Satellite Facility repository. The cGPS timeseries solutions used are freely accessible on the Nevada Geodetic Laboratory repository. The water data used are included in Carrera-Hernandez and Gaskin (2007), Lesser and Gonzalez-Posadas (2005) and Ruiz (2015). Well locations and pumping rates are included in Carrera-Hernandez and Gaskin (2007). Fault and fissure data are included in Carreón-Freyre et al. (2017). Socioeconomic data used in this study are included in Tortajada (2006a). Aquifer and aquitard thicknesses are from Gobierno del Distrito Federal (2004). Land use data are from the "Centro de Investigación en Ciencias de Información Geoespacial" (CONACYT, 2020) and population density data are from the "Facebook Connectivity Lab and Center for International Earth Science Information Network - CIESIN - Columbia University (2016)." The ISCE and GMTSAR processing are open source software freely available from WInSAR and Github. MintPy is an open source software distributed on Github.

Acknowledgments
GPS data are part of the Trans-boundary, Land, and Atmosphere Long-term Observational and Collaborative Network (TLALOCNet) operated by the Servicio de Geodesia Satelital (SGS) at the Instituto de Geofísica-Universidad Nacional Autónoma de México (UNAM) in collaboration with UNAVCO and with support from the National Science Foundation and the National Aeronautics and Space Administration under NSF Cooperative Agreement EAR-1724794 and by NOAA-NGS. The authors thank Luis Salazar Tlaczani at SGS and all the personnel from UNAVCO Inc. for station maintenance, data acquisition, IT support, and data distribution for these networks. TLALOCNet and related SGS operations are supported by the National Science Foundation Number EAR-1338091 and Consejo Nacional de Ciencia y Tecnología (CONACyT) projects 253760, 256012, and 2017-01-5955, UNAM-Programa de Apoyo a Proyectos de Investigación e Innovación Tecnológica (PAPIIT) projects IN104213, IN111509, IN109315-3, IN104818-3, IN107321, and supplemental support from UNAM-Instituto de Geofísica.
This work benefited from access to the University of Oregon high-performance computer, Talapas. The first author (E. Chaussard) is supported by the National Aeronautics and Space Administration through grant number 80NSSC19K0741. E. Cabral-Cano acknowledges support from PAPIIT project IN104818-3, IN107321, and CONACyT projects 256012 and 2017-01-5955. Part of the research was carried out at the Jet Propulsion Laboratory, California Institute of Technology, under a contract with the National Aeronautics and Space Administration. The authors thank the Associate Editor and Editor for their constructive feedback.

References

Abdollahi, S., Pourghasemi, H. R., Ghanbarian, G. A., & Safaeian, R. (2019). Prioritization of effective factors in the occurrence of land subsidence and its susceptibility mapping using an SVM model and their different kernel functions. *Bulletin of Engineering Geology and the Environment*, *78*, 4017–4034. https://doi.org/10.1007/s10064-018-1403-6

Alberto-Jaime, P., & Méndez-Sánchez, E. (2010). Evolution of Mexico City clay properties affected by land subsidence. In D. Carreón-Freyre, M. Cerca, D. L. Galloway, & J. J. Silva-Corona (Eds.), *Land subsidence, associated hazards and the role of natural resources development* (*339*, p. 522). Wallingford, UK: International Association of Hydrological Sciences.

Amelung, F., Galloway, D. L., Bell, J. W., Zebker, H. A., & Laczniak, R. J. (1999). Sensing the ups and downs of Las Vegas: InSAR reveals structural control of land subsidence and aquifer-system deformation. *Geology*, *27*, 483–486. https://doi.org/10.1130/0091-7613(1999)027<0483:stuado>2.3.co;2

Auvinet, G., & Juarez, M. (2002). Geostatistical characterization and simulation of Mexico Valley subsoil. In *Applied modelling and simulation* (pp. 208–212), IASTED.

Bell, J. W., Amelung, F., Ferretti, A., Bianchi, M., & Novali, F. (2008). Permanent scatterer InSAR reveals seasonal and long-term aquifer-system response to groundwater pumping and artificial recharge. *Water Resources Research*, *44*. https://doi.org/10.1029/2007wr006152

Birkle, P., Torres, V., & Gonzalez, E. (1995). Preliminary evaluation of the potential of deep aquifers in the Mexican Valley Basin. *Ingenieria Hidraulica en Mexico*, *10*, 47–53.

Blewitt, G., Hammond, W. C., & Kreemer, C. (2018). Harnessing the GPS data explosion for interdisciplinary science. *Eos*, *99*. https://doi.org/10.1029/2018eo104623

Bürgmann, R., Rosen, P. A., & Fielding, E. J. (2000). Synthetic aperture radar interferometry to measure Earth's surface topography and its deformation. *Annual Review of Earth and Planetary Sciences*, *28*, 169–209. https://doi.org/10.1146/annurev.earth.28.1.169

Cabral-Cano, E., Dixon, T. H., Miralles-Wilhelm, F., Díaz-Molina, O., Sánchez-Zamora, O., & Carande, R. E. (2008). Space geodetic imaging of rapid ground subsidence in Mexico City. *The Geological Society of America Bulletin*, *120*, 1556–1566. https://doi.org/10.1130/b26001.1

Cabral-Cano, E., Osmanoglu, B., Dixon, T., Wdowinski, S., DeMets, C., Cigna, F., & Díaz-Molina, O. (2010). Subsidence and fault hazard maps using PSI and permanent GPS networks in central Mexico. In *Proceedings of the eighth international symposium on land subsidence* (pp. 17–22) Querétaro, Mexico.

Cabral-Cano, E., Pérez-Campos, X., Márquez-Azúa, B., Sergeeva, M. A., Salazar-Tlaczani, L., DeMets, C., et al. (2018). TLALOCNet: A continuous GPS-Met backbone in Mexico for seismotectonic and atmospheric research. *Seismological Research Letters*, *89*, 373–381. https://doi.org/10.1785/0220170190

Cabral-Cano, E., Solano-Rojas, D., Oliver-Cabrera, T., Wdowinski, S., Chaussard, E., Salazar-Tlaczani, L., et al. (2015). Satellite geodesy tools for ground subsidence and associated shallow faulting hazard assessment in central Mexico. *Proceedings of the international association of hydrological sciences* (*372*, pp. 255–260). https://doi.org/10.5194/piahs-372-255-2015

Calderhead, A. I., Martel, R., Garfias, J., Rivera, A., & Therrien, R. (2012a). Sustainable management for minimizing land subsidence of an over-pumped volcanic aquifer system: Tools for policy design. *Water Resources Management*, *26*, 1847–1864. https://doi.org/10.1007/s11269-012-9990-7

Calderhead, A. I., Martel, R., Garfias, J., Rivera, A., & Therrien, R. (2012b). Pumping dry: An increasing groundwater budget deficit induced by urbanization, industrialization, and climate change in an over-exploited volcanic aquifer. *Environmental Earth Sciences*, *66*, 1753–1767. https://doi.org/10.1007/s12665-011-1398-9

Calderhead, A. I., Therrien, R., Rivera, A., Martel, R., & Garfias, J. (2011). Simulating pumping-induced regional land subsidence with the use of InSAR and field data in the Toluca Valley, Mexico. *Advances in Water Resources*, *34*, 83–97. https://doi.org/10.1016/j.advwatres.2010.09.017

Cardona, A., & Hernández, N. (1995). Modelo geoquímico conceptual de la evolución del agua subterránea en el Valle de México. *Tecnologia y Ciencias del agua*, *10*, 71–90.

Carreón-Freyre, D., Cerca, M., Gutiérrez-Calderón, R., López-Quiroz, P., Alcántara-Durán, C., González-Hernández, M., & Centeno-Salas, F. (2017). *Posible influencia de la subsidencia y fracturamiento en la Ciudad de México en las construcciones dañadas por el sismo del 19 de Septiembre de 2017* (p. 13). Geociencias. Retrieved from http://www1.cenapred.unam.mx/SUBCUENTA/22a%20SESIÓN%20ORDINARIA/VIII.%20ASUNTOS%20GENERALES/Reporte%20CDMX%20sismo%202017.pdf

Carrera-Hernández, J. J., & Gaskin, S. J. (2007). Spatio temporal analysis of daily precipitation and temperature in the Basin of Mexico. *Journal of Hydrology*, *336*, 231–249. https://doi.org/10.1016/j.jhydrol.2006.12.021

Carrillo, N. (1948). Influence of artesian wells in the sinking of Mexico City. *Proceedings of the second international conference on soil mechanics and foundation engineering* (*7*, 156–159). Rotterdam, Holland: International Society for Soil Mechanics and Geotechnical Engineering.

Castellazzi, P., Garfias, J., Martel, R., Brouard, C., & Rivera, A. (2017). InSAR to support sustainable urbanization over compacting aquifers: The case of Toluca Valley, Mexico. *International Journal of Applied Earth Observation and Geoinformation*, *63*, 33–44. https://doi.org/10.1016/j.jag.2017.06.011

Castellazzi, P., Longuevergne, L., Martel, R., Rivera, A., Brouard, C., & Chaussard, E. (2018). Quantitative mapping of groundwater depletion at the water management scale using a combined GRACE/InSAR approach. *Remote Sensing of Environment*, *205*, 408–418. https://doi.org/10.1016/j.rse.2017.11.025

Chaussard, E., Amelung, F., Abidin, H., & Hong, S.-H. (2013). Sinking cities in Indonesia: ALOS PALSAR detects rapid subsidence due to groundwater and gas extraction. *Remote Sensing of Environment*, *128*, 150–161. https://doi.org/10.1016/j.rse.2012.10.015

Chaussard, E., Bürgmann, R., Fattahi, H., Johnson, C. W., Nadeau, R., Taira, T., & Johanson, I. (2015a). Interseismic coupling and refined earthquake potential on the Hayward-Calaveras fault zone. *Journal of Geophysical Research: Solid Earth*, *120*, 8570–8590. https://doi.org/10.1002/2015jb012230

Chaussard, E., Bürgmann, R., Fattahi, H., Nadeau, R. M., Taira, T., Johnson, C. W., & Johanson, I. (2015b). Potential for larger earthquakes in the East San Francisco Bay Area due to the direct connection between the Hayward and Calaveras faults. *Geophysical Research Letters*, *42*, 2734–2741. https://doi.org/10.1002/2015gl063575

Chaussard, E., Bürgmann, R., Shirzaei, M., Fielding, E. J., & Baker, B. (2014). Predictability of hydraulic head changes and characterization of aquifer-system and fault properties from InSAR-derived ground deformation. *Journal of Geophysical Research: Solid Earth*, *119*, 6572–6590. https://doi.org/10.1002/2014jb011266

Chaussard, E., & Farr, T. G. (2019). A new method for isolating elastic from inelastic deformation in aquifer systems: Application to the San Joaquin Valley, CA. *Geophysical Research Letters*, *46*, 10800–10809. https://doi.org/10.1029/2019gl084418

Chaussard, E., Johnson, C. W., Fattahi, H., & Bürgmann, R. (2016). Potential and limits of InSAR to characterize interseismic deformation independently of GPS data: Application to the southern San Andreas Fault system. *Geochemistry, Geophysics, Geosystems*, *17*, 1214–1229. https://doi.org/10.1002/2015gc006246

Chaussard, E., Milillo, P., Bürgmann, R., Perissin, D., Fielding, E. J., & Baker, B. (2017). Remote sensing of ground deformation for monitoring groundwater management practices: Application to the Santa Clara Valley during the 2012-2015 California drought. *Journal of Geophysical Research: Solid Earth*, *122*, 8566–8582. https://doi.org/10.1002/2017jb014676

Chaussard, E., Wdowinski, S., Cabral-Cano, E., & Amelung, F. (2014). Land subsidence in central Mexico detected by ALOS InSAR time-series. *Remote Sensing of Environment*, *140*, 94–106. https://doi.org/10.1016/j.rse.2013.08.038

Chelleri, L., Schuetze, T., & Salvati, L. (2015). Integrating resilience with urban sustainability in neglected neighborhoods: Challenges and opportunities of transitioning to decentralized water management in Mexico City. *Habitat International*, *48*, 122–130. https://doi.org/10.1016/j.habitatint.2015.03.016

Chen, C. W., & Zebker, H. A. (2002). Phase unwrapping for large SAR interferograms: Statistical segmentation and generalized network models. *IEEE Transactions on Geoscience and Remote Sensing*, *40*, 1709–1719. https://doi.org/10.1109/tgrs.2002.802453

Cigna, F., Cabral-Cano, E., Osmanoğlu, B., Dixon, T. H., & Wdowinski, S. (2011). Detecting subsidence-induced faulting in Mexican urban areas by means of persistent scatterer interferometry and subsidence horizontal gradient mapping. In *2011 IEEE international geoscience and remote sensing symposium* (pp. 2125–2128), IEEE.

Cigna, F., & Tapete, D. (2021). Present-day land subsidence rates, surface faulting hazard and risk in Mexico City with 2014-2020 Sentinel-1 IW InSAR. *Remote Sensing of Environment*, *253*, 112161. https://doi.org/10.1016/j.rse.2020.112161

CONACYT. (2020). *Centro de Investigación en Ciencias de Información Geoespacial*. Retrieved from https://centrosconacyt.mx/centro-publico/centrogeo/

CONAGUA. (2009). *Situación del Subsector Agua Potable, Alcantarillado y Saneamiento*. Comisión Nacional del Agua (CONAGUA). Retrieved from http://www.conagua.gob.mx/CONAGUA07/Publicaciones/Publicaciones/LibroAnexosYTablas-Situaci%C3%B3nSAPAS.pdf

Cuevas, J. (1936). Foundation conditions in Mexico City. *International conference on soil mechanics and foundation engineering*, (*3*, pp. 233–237).

Davila-Hernandez, N., Madrigal, D., Exposito, J. L., & Antonio, X. (2014). Multi-temporal analysis of land subsidence in Toluca Valley (Mexico) through a combination of persistent scatterer interferometry (PSI) and historical piezometric data. *Advances in Remote Sensing*, *3*, 49–60. https://doi.org/10.4236/ars.2014.32005

Del Campo, M. M., Esteller, M. V., Expósito, J. L., & Hirata, R. (2014). Impacts of urbanization on groundwater hydrodynamics and hydrochemistry of the Toluca Valley aquifer (Mexico). *Environmental Monitoring and Assessment*, *186*, 2979–2999. https://doi.org/10.1007/s10661-013-3595-3

Du, Z., Ge, L., Ng, A. H. M., Zhu, Q., Zhang, Q., Kuang, J., & Dong, Y. (2019). Long-term subsidence in Mexico City from 2004 to 2018 revealed by five synthetic aperture radar sensors. *Land Degradation and Development*, *30*, 1785–1801. https://doi.org/10.1002/ldr.3347

Durazo, J., & Farvolden, R. N. (1989). The groundwater regime of the Valley of Mexico from historic evidence and field observations. *Journal of Hydrology*, *112*, 171–190. https://doi.org/10.1016/0022-1694(89)90187-x

Esteller, M. V., & Andreu, J. M. (2005). Anthropic effects on hydrochemical characteristics of the Valle de Toluca aquifer (central Mexico). *Hydrogeology Journal*, *13*, 378–390. https://doi.org/10.1007/s10040-004-0395-4

Esteller, M. V., Rodríguez, R., Cardona, A., & Padilla-Sánchez, L. (2012). Evaluation of hydrochemical changes due to intensive aquifer exploitation: Case studies from Mexico. *Environmental Monitoring and Assessment*, *184*, 5725–5741. https://doi.org/10.1007/s10661-011-2376-0

Facebook Connectivity Lab and Center for International Earth Science Information Network - CIESIN - Columbia University. (2016). *High resolution settlement layer (HRSL). Source imagery for HRSL © 2016 DigitalGlobe*. Retrieved from https://ciesin.columbia.edu/data/hrsl/

Fattahi, H., Agram, P., & Simons, M. (2017). A network-based enhanced spectral diversity approach for TOPS time-series analysis. *IEEE Transactions on Geoscience and Remote Sensing*, *55*, 777–786. https://doi.org/10.1109/tgrs.2016.2614925

Fattahi, H., & Amelung, F. (2013). DEM error correction in InSAR time series. *IEEE Transactions on Geoscience and Remote Sensing*, *51*, 4249–4259. https://doi.org/10.1109/tgrs.2012.2227761

Fernández-Torres, E., Cabral-Cano, E., Solano-Rojas, D., Havazli, E., and Salazar-Tlaczani, L. (2020). Land Subsidence risk maps and InSAR based angular distortion structural vulnerability assessment: An example in Mexico City. *Proceedings of the International Association of Hydrological Sciences*, *382*, 583–587. https://doi.org/10.5194/piahs-382-583-2020

Figueroa-Vega, G. E. (1984). Case history No. 9.8, Mexico, DF, Mexico. In J. Poland (Ed.), *Guidebook to studies of land subsidence due to ground-water withdrawal: Studies and reports in hydrology* (*40*, pp. 217–232), UNESCO.

Freeze, R. A., & Cherry, J. A. (1979). *Groundwater* (p. 604). Englewood Cliffs, NJ: Prentice-Hall.

Gayol, R. (1929). Breves apuntes relativos a las obras de saneamiento y desague de la capital de la republica y de las que, del mismo genero necesita con urgencia. *Revista Mexicana de Ingenieria y Arquitectura*, *8*.

Gobierno de la Ciudad de Mexico. (2019). *Decreto por el que se reforman, adicionan y derogan diversas disposiciones del Reglamento de Construcciones para el Distrito Federal. Gaceta Oficial de la Ciudad de México, 21 época, 2 Abril 2019, No. 63 Bis* (p. 12).

Gobierno del Distrito Federal. (2004). *Normas técnicascomplementarias del reglamento de construcciones del distritofederal. Tomo II: Normas técnicas complementarias sobre criterios y acciones para el diseño estructural de las edificaciones, cimentaciones, viento,sismo, hidráulicas, arquitec. Gaceta Oficial del Distrito Federal, 14 época, 6 de Octubre 2004, Tomo II, No. 103- Bis* (p. 302). Retrieved from http://www.paot.org.mx/centro/gaceta/Octubre2004.html

Gualandi, A., Avouac, J.-P., Galetzka, J., Genrich, J. F., Blewitt, G., Adhikari, L. B., et al. (2017). Pre- and post-seismic deformation related to the 2015, Mw7.8 Gorkha earthquake, Nepal. *Tectonophysics*, *714–715*, 90–106. https://doi.org/10.1016/j.tecto.2016.06.014

Hernández-Espriú, A., Arango-Galván, C., Reyes-Pimentel, A., Martínez-Santos, P., Pita de la Paz, C., Macías-Medrano, S., et al. (2017). Water supply source evaluation in unmanaged aquifer recharge zones: The Mezquital Valley (Mexico) case study. *Water*, *9*, 4. https://doi.org/10.3390/w9010004

Hernández-Espriú, A., Reyna-Gutiérrez, J. A., Sánchez-León, E., Cabral-Cano, E., Carrera-Hernández, J., Martínez-Santos, P., et al. (2014). The DRASTIC-Sg model: An extension to the DRASTIC approach for mapping groundwater vulnerability in aquifers subject to differential land subsidence, with application to Mexico City. *Hydrogeology Journal*, *22*, 1469–1485. https://doi.org/10.1007/s10040-014-1130-4

Holzer, T. L., & Johnson, A. I. (1985). Land subsidence caused by ground watergroundwater withdrawal in urban areas. *GeoJournal*, *11*, 245–255. https://doi.org/10.1007/bf00186338

Huizar-Alvarez, R., Carrillo-Rivera, J. J., Angeles-Serrano, G., Hergt, T., & Cardona, A. (2004). Chemical response to groundwater extraction southeast of Mexico City. *Hydrogeology Journal*, *12*, 436–450. https://doi.org/10.1007/s10040-004-0343-3

Hyvärinen, A., & Oja, E. (1997). A fast fixed-point algorithm for independent component analysis. *Neural Computation*, *9*, 1483–1492. https://doi.org/10.1162/neco.1997.9.7.1483

Jolivet, R., Agram, P. S., Lin, N. Y., Simons, M., Doin, M. P., Peltzer, G., & Li, Z. (2014). Improving InSAR geodesy using global atmospheric models. *Journal of Geophysical Research: Solid Earth*, *119*, 2324–2341. https://doi.org/10.1002/2013jb010588

Lesser, J. M., & González-Posadas, D. (2005). El agua subterránea de la Ciudad de México‖. In *V congreso de Aguas subterráneas*. Hermosillo, Son. Lesser y Asociados, SA.

Lesser y Asociados. (2003). *Mapa de niveles estáticos con base en información del Sistema de Aguas de la Ciudad de México durante agosto 2002* (p. 200).

López-Quiroz, P., Doin, M.-P., Tupin, F., Briole, P., & Nicolas, J.-M. (2009). Time series analysis of Mexico City subsidence constrained by radar interferometry. *Journal of Applied Geophysics*, *69*, 1–15. https://doi.org/10.1016/j.jappgeo.2009.02.006

Mazari-Hiriart, M., Tapia-Palacios, M. A., Zarco-Arista, A. E., & Espinosa-García, A. C. (2019). Challenges and opportunities on urban water quality in Mexico City. *Frontiers in Environmental Science*, *7*, 169. https://doi.org/10.3389/fenvs.2019.00169

Mazari, M., & Alberro, J. (1991). Hundimiento de la Ciudad de Mexico. In M. Mazari, & J. Kumate (Eds.), *Los problemas de la Cuenca de Mexico* (p. 403). Mexico City: El Colegio Nacional.

Mejía, L., Murillo, S., & Reyes, J. (2007b). *Plan de manejo del Valle de Toluca. Cuenca y Acuífero. Problemática y Perspectivas. Subdirección General de Programación; Dirección Local Estado de México*. CONAGUA (Comisión Nacional del Agua).

Miller, M. M., & Shirzaei, M. (2015). Spatiotemporal characterization of land subsidence and uplift in Phoenix using InSAR time series and wavelet transforms. *Journal of Geophysical Research: Solid Earth*, *120*, 5822–5842. https://doi.org/10.1002/2015jb012017

Mooser, F., Montiel, A., & Zúñiga, A. (1996). *Nuevo mapa geológico de las cuencas de México, toluca y Puebla, estratigrafía, tectónica regional y aspectos geotérmicos [new geologic map of the basins of Mexico, toluca and Puebla: Stratigraphy, regional tectonic and geothermal aspects]* (p. 63). Comisión Federal de Electricidad.

Morales-Casique, E., Zapata Norberto, B., & Herrera, G. S. (2018). Estimating vertical hydraulic conductivity and land subsidence during one-dimensional nonlinear groundwater flow and consolidation in highly compressible aquitards by Ensemble Kalman Filter. *American Geophysical Union, Fall Meeting Abstracts 2018*. Retrieved from https://fallmeeting.agu.org/2018/

Motagh, M., Walter, T. R., Sharifi, M. A., Fielding, E., Schenk, A., Anderssohn, J., & Zschau, J. (2008). Land subsidence in Iran caused by widespread water reservoir overexploitation. *Geophysical Research Letters*, *35*. https://doi.org/10.1029/2008gl033814

National Research Council (1995). *Mexico City's water supply: Improving the outlook for sustainability*. Washington, DC: National Academy Press. Retrieved from http://lanic.utexax.edu/la/Mexico/water/book.html

Neuman, S. P., & Witherspoon, P. A. (1969). Theory of flow in a confined two aquifer system. *Water Resources Research*, *5*, 803–816. https://doi.org/10.1029/wr005i004p00803

Niederberger, C. (1987). *Paléopaysages et archéologie pré-urbaine du bassin de México (Mexique)* (p. 357). Centre d'études mexicaines et centraméricaines.

Ortega, A. G., & Farvolden, R. N. (1989). Computer analysis of regional groundwater flow and boundary conditions in the Basin of Mexico. *Journal of Hydrology*, *110*, 271–294. https://doi.org/10.1016/0022-1694(89)90192-3

Ortega-Guerrero, A., Cherry, J. A., & Rudolph, D. L. (1993). Large-scale aquitard consolidation near Mexico City. *Groundwater*, *31*, 708–718.

Ortega-Guerrero, A., Rudolph, D. L., & Cherry, J. A. (1999). Analysis of long-term land subsidence near Mexico City: Field investigations and predictive modeling. *Water Resources Research*, *35*, 3327–3341. https://doi.org/10.1029/1999wr900148

Ortiz Zamora, D., & Ortega Guerrero, A. (2010). Evolution of long-term land subsidence near Mexico City: Review, field investigations, and predictive simulations. *Water Resources Research*, *46*. https://doi.org/10.1029/2008WR007398

Osmanoğlu, B., Dixon, T. H., Wdowinski, S., Cabral-Cano, E., & Jiang, Y. (2011). Mexico City subsidence observed with persistent scatterer InSAR. *International Journal of Applied Earth Observation and Geoinformation*, *13*, 1–12. https://doi.org/10.1016/j.jag.2010.05.009

Pavelko, M. T. (2004). *Estimates of hydraulic properties from a one-dimensional numerical model of vertical aquifer-system deformation Lorenzi site, Las Vegas, Nevada* (p. 52). US Department of the Interior, US Geological Survey. https://doi.org/10.3133/wri034083

Pérez-Rocha, L. E., Ordaz, M., & Sánchez-Sesma, F. J. (1995). Spatial interpolation of seismic data: The case of the Valley of Mexico. In *Proceedings of the 10th pan-American conference on soil mechanics and foundation engineering*. Retrieved from http://classify.oclc.org/classify2/ClassifyDemo?owi=5612459551

Poland, J. F., & Ireland, R. L. (1988). *Land subsidence in the Santa Clara Valley, California, as of 1982* (p. 93). Department of the Interior, US Geological Survey. https://doi.org/10.3133/ofr84818

Riley, F. S. (1998). Mechanics of aquifer systems—The scientific legacy of Joseph F. Poland. In J. W. Borchers (Ed.), *Land subsidence: Case studies and current Research, proceedings of the Dr. Joseph F. Poland symposium on land subsidence* (pp. 13–27). Association of Engineering Geologists Special Publications.

Rosen, P. A., Gurrola, E. M., Agram, P. S., Sacco, G. F., & Lavalle, M. (2015). The InSAR Scientific Computing Environment (ISCE): A python framework for Earth science. In *American Geophysical Union, fall meeting abstracts 2015*. Retrieved from https://agu.confex.com/agu/fm15/meetingapp.cgi/Paper/60264

Rudolph, D. L., Cherry, J. A., & Farvolden, R. N. (1991). Groundwater flow and solute transport in fractured lacustrine clay near Mexico City. *Water Resources Research*, *27*, 2187–2201. https://doi.org/10.1029/91wr01306

Rudolph, D. L., Sultan, R., Garfias, J., & McLaren, R. G. (2006). Significance of enhanced infiltration due to groundwater extraction on the disappearance of a headwater lagoon system: Toluca Basin, Mexico. *Hydrogeology Journal*, *14*, 115–130. https://doi.org/10.1007/s10040-005-0463-4

Ruiz, G. (2015). Estimation of the groundwater recharge in the aquifer of the Mexico City. *Procedia Environmental Sciences*, *25*, 220–226. https://doi.org/10.1016/j.proenv.2015.04.030

Sahakian, V. J., Melgar, D., Quintanar, L., Ramírez-Guzmán, L., Pérez-Campos, X., & Baltay, A. (2018). Ground motions from the 7 and 19 September 2017 Tehuantepec and Puebla-Morelos, Mexico, earthquakes. *Bulletin of the Seismological Society of America*, *108*, 3300–3312. https://doi.org/10.1785/0120180108

Samsonov, S. V., & d'Oreye, N. (2017). Multidimensional small baseline subset (MSBAS) for two-dimensional deformation analysis: Case study Mexico City. *Canadian Journal of Remote Sensing*, *43*, 318–329. https://doi.org/10.1080/07038992.2017.1344926

Santoyo, M. A., Singh, S. K., & Mikumo, T. (2005). Source process and stress change associated with the 11 January, 1997 (Mw= 7.1) Michoácan, Mexico, inslab earthquake. *Geofísica Internacional*, *44*, 317–330.

Sistema de Aguas de la Ciudad de México. (2012). *El gran reto del agua en la Ciudad de México. Pasado, presente y prospectivas de solución para una de las ciudades más complejas del mundo*. Sistema de Aguas de la Ciudad de México.

Solano-Rojas, D., Cabral-Cano, E., Fernández-Torres, E., Havazli, E., Wdowinski, S., and Salazar-Tlaczani, L. (2020b). Remotely triggered subsidence acceleration in Mexico City induced by the September 2017 Mw 7.1 Puebla and the Mw 8.2 Tehuantepec September 2017 earthquakes. *Proceedings of the International Association of Hydrological Sciences*, *382*, 683–687. https://doi.org/10.5194/piahs-382-683-2020

Solano Rojas, D., Cabral Cano, E., Hernández Espriú, A., Wdowinski, S., DeMets, C., Salazar Tlaczani, L., et al. (2015). La relación de subsidencia del terreno InSAR-GPS y el abatimiento del nivel estático en pozos de la zona Metropolitana de la Ciudad de México. *Boletin de la Sociedad Geologica Mexicana*, *67*, 273–283. https://doi.org/10.18268/bsgm2015v67n2a10

Solano-Rojas, D. E., Wdowinski, S., Cabral-Cano, E., Osmanoglu, B., Havazli, E., and Pacheco-Martínez, J. (2020a). A multiscale approach for detection and mapping differential subsidence using multi-platform InSAR products. *Proceedings of the International Association of Hydrological Sciences*, *382*, 173–177. https://doi.org/10.5194/piahs-382-173-2020

Stead, D., & Pojani, D. (2017). The urban transport crisis in emerging economies: A comparative overview. *The urban transport crisis in emerging economies* (pp. 283–295). https://doi.org/10.1007/978-3-319-43851-1_14

Strozzi, T., & Wegmuller, U. (1999). Land subsidence in Mexico City mapped by ERS differential SAR interferometry. *IEEE 1999 international geoscience and remote sensing symposium* (pp. 1940–1942), IEEE. https://doi.org/10.1109/IGARSS.1999.774993

Terzaghi, K., Peck, R. B., & Mesri, G. (1996). *Soil mechanics in engineering practice* (p. 592). John Wiley and Sons.

Tien Bui, D., Shahabi, H., Shirzadi, A., Chapi, K., Pradhan, B., Chen, W., et al. (2018). Land subsidence susceptibility mapping in South Korea using machine learning algorithms. *Sensors*, *18*, 2464. https://doi.org/10.3390/s18082464

Tortajada, C. (2006a). Water management in Mexico City metropolitan area. *Water Resources Development*, *22*, 353–376. https://doi.org/10.1080/07900620600671367

Tortajada, C. (2006b). *Who has access to water? Case study of Mexico City metropolitan area (No. HDOCPA-2006-16)* (p. 47). Human Development Report Office (HDRO), United Nations Development Programme (UNDP).

Viens, L., Denolle, M. A., Hirata, N., & Nakagawa, S. (2018). Complex near-surface rheology inferred from the response of greater Tokyo to strong ground motions. *Journal of Geophysical Research: Solid Earth*, *123*, 5710–5729. https://doi.org/10.1029/2018jb015697

Wilson, A. M., & Gorelick, S. (1996). The effects of pulsed pumping on land subsidence in the Santa Clara Valley, California. *Journal of Hydrology*, *174*, 375–396. https://doi.org/10.1016/0022-1694(95)02722-x

Yunjun, Z., Fattahi, H., & Amelung, F. (2019). Small baseline InSAR time series analysis: Unwrapping error correction and noise reduction. *Computers & Geosciences*, *133*, 104331. https://doi.org/10.1016/j.cageo.2019.104331